Contents lists available at ScienceDirect

Applied Catalysis B: Environmental

PtCo/CoO$_x$ nanocomposites: Bifunctional electrocatalysts for oxygen reduction and evolution reactions synthesized via tandem laser ablation synthesis in solution-galvanic replacement reactions

Sheng Hu [b,d], Gabriel Goenaga [b,d], Chad Melton [c], Thomas A. Zawodzinski [b,d], Dibyendu Mukherjee [a,b,d,∗]

[a] Department of Mechanical, Aerospace, and Biomedical Engineering, University of Tennessee, Knoxville, TN 37996, United States
[b] Department of Chemical and Biomolecular Engineering, University of Tennessee, Knoxville, TN 37996, United States
[c] Department of Physics, University of Tennessee, Knoxville, TN 37996, United States
[d] Sustainable Energy Education and Research Center (SEERC), University of Tennessee, Knoxville, TN 37996, United States

ARTICLE INFO

ABSTRACT

Efficient yet, low-cost electrocatalysts are indispensable for electrochemical oxygen reduction reactions (ORR) and oxygen evolution reactions (OER). Here we present laser ablation synthesis in solution in tandem with galvanic replacement reaction (LASiS–GRR), for the first time, as a facile route to synthesize nanocomposites (NCs) of PtCo nanaoalloy (NA) embedded in CoO$_x$ matrices as bifunctional electrocatalysts. High resolution TEM reveals PtCo NA of mean sizes ∼8.5–17.7 nm embedded in sponge-shaped CoO$_x$ matrices, while electron diffraction and X-ray diffraction data along with energy dispersive X-ray spectrometry (EDX) confirm the NC compositions and crystalline structures. Detailed electrochemistry data indicates outstanding ORR and OER activities for the PtCo/CoO$_x$ NCs while exhibiting better stability than the respective standard nanocatalysts. Such activities are ascribed to the shrunken lattice constants of alloyed PtCo that promote oxygen adsorption and the synergic "spillover" effect from high surface area CoO$_x$ matrices that accelerate both ORR and OER through symbiotic adsorption/desorption of intermediate species, while preventing aggregation and/or dissolution in alkaline medium. We report a combined overpotential of 756 mV vs. RHE for the PtCo/CoO$_x$ NC with 33.3% (molar) Pt content which is the best value ever reported for catalysts supported by carbon black. The enhanced bifunctional catalytic activities of the NCs are attributed to their unique heteronanostructures tailored by our one-pot, "green" synthesis route of LASiS–GRR.

1. Introduction

Increasing demand for sustainable energy has escalated the research on clean, highly efficient and environmentally benign energy conversion and storage technologies [1–3]. To this end, state-of-the-art renewable energy generation and storage systems such as regenerative proton exchange membrane fuel cells (PEM-FCs) and metal–air batteries have gained tremendous interest. Yet, both these systems involve sluggish electrochemical reactions in the cathode due to the complicated four electron transfer processes involved in the oxygen reduction (ORR) and oxygen evolution

reactions (OER) for the discharging and charging process respectively [3–10]. As a consequence, in the past decades or so, various nanoparticle (NP) based catalysts have been extensively researched and developed in an effort to efficiently and economically enhance the aforementioned reactions [4,5,11–14].

Typically, Pt-based NPs are widely used as efficient catalysts to provide complete four-electron transport pathways with remarkably reduced overpotentials during ORR processes in PEMFCs and other electrochemical systems [8,11,15–17]. However, the high cost and poor stability of Pt under harsh alkaline or, acidic conditions of electrochemical cells [18] has led to the search for active non-precious metal/metal oxide catalysts that can replace Pt [4,8,19–21]. To this end, recent years have seen a surge in mixed valence oxides of transition metals with spinel structures (Co$_3$O$_4$, Mn$_3$O$_4$, NiO, etc.) as electrocatalysts, in spite of their catalytic activ-

ities being relatively low [4,21–23]. In addition, Pt–M nanoalloys with various atomic structures, and morphologies have been shown to manifest similar or even better ORR catalytic performances than Pt [11,12,21,24–26]. The improved activity is attributed to the combination of geometric and electronic effects where the former refers to the shrunken Pt lattice constants while, the latter refers to higher 5d orbital vacancies in the electronic structure of Pt–M alloys [11,21]. Recently, much progress has been made for the Pt–M nanoalloy systems. New methods have been developed for synthesizing various shaped Pt–M nanostructures including seed-mediated approach, solid-state chemical enabled scalable production to name a few [27–31]. More specifically, there has been previous reports on the synthesis of Mo-doped Pt_3Ni octahedral as superior ORR catalysts [32], and systematic anisotropic growth of shaped nanoalloys of Pt–Ni and Pt–Co that play significant role on their catalytic properties [33].

On the other hand, OER plays a critical role in water splitting processes during solar fuel production, or, charge–discharge processes in rechargeable fuel cells and batteries [3,13,14,34]. Hence, electrodes in ideal regenerative electrochemical devices should have high conversion rates for both ORR and OER processes. Unlike the ORR systems, transition metal oxides (e.g., CoO_x, NiO_x, TiO_2, IrO_2, etc.) or perovskites are typically considered as excellent catalytic candidates for OER on account of their high activities and good photo-stability [35–41]. The key challenge in the design of ideal reversible electrodes is in the low-cost, reproducible synthesis of bi-functional catalysts that can outperform both the ORR and OER activities of commercially available electrocatalysts. A few recent attempts have synthesized designer nanocomposites (NCs) made from the best of both ORR (Pt NPs) and OER catalysts (transition metal oxides) that make use of the synergic "spillover" effects to influence the adsorption/desorption behavior of intermediate species at the catalyst surfaces, thereby driving the rate determining steps in each of the respective reactions [42–44].

However, clean synthesis of these complex nanocatalysts in a facile, cheap, and reproducible manner still remains elusive. Most synthesis techniques for metal and metal oxide NPs involve wet chemical routes that require intricate experimental steps involving indispensable chemicals such as surfactants, organic ligands, reducing agents, etc. that block their active surface catalytic sites [10,11,25,45]. Many metal/metal oxide NCs are made from perkovsite based oxides that are complicated to synthesize and require multi-step processes with harsh chemical conditions and residues [38,39,44]. Finally, removal of organic encapsulation (ligands and/or surfactants) from metal/metal oxide NPs itself is a challenging and critical step in their preparation [46].

Laser ablation synthesis in solution (LASiS) offers a "green", facile route for one-step synthesis of complex nanomaterials without the use of harsh reducing agents and/or, surfactants/ligands. LASiS has gained tremendous interests in recent years as an elegant, efficient, and easily operable synthesis technique for producing various nanomaterials with low start-up costs [47–49]. Such interests have led to the use of LASiS to produce various NPs of heavy metals [50,51], transition metals [47,52], intermetallic composites [53,54], including core–shell [55,56], and hollow [57] structures. As schematically represented in Fig. 1 and studied elsewhere in details [58], LASiS involves an expanding liquid-confined plasma plume with exceedingly high temperatures and pressures that thermally vaporizes a metal target and produces a shock wave with cavitation bubbles. The bubbles containing supersaturated seeding NPs (i.e., the vapor pressure of the ablated species is larger than the equilibrium pressure) then oscillates and expands at a supersonic speed (>10^3 m/s) up to a radius of the order of millimeters within 10^{-4} s. After which the bubbles quickly collapse with the inside seeding NPs undergoing ultrafast collisional quenching at the bubble–liquid interface [59,60]. The inherent charge screening effects within the plasma promotes the production of uniformly dispersed colloidal NPs [61] without the need for any surfactants/stabilizing agents that are usually indispensable in chemical synthesis routes and yet, potentially harmful for surface catalytic activities. However, the perceived drawback for LASiS has been in its inability to accurately control the structure and morphology of the synthesized nanomaterials [60]. Although our recent work demonstrated the ability of LASiS to tailor size, morphology and composition of cobalt oxide/hydroxide NPs [58], the ability of chemical reduction kinetics to provide superior control on NP composition and morphology (especially, for binary or ternary intermetallic NPs) cannot be undermined. Hence, we hypothesize that the extreme physicochemical conditions of LASiS [58], when interfaced with chemical reduction routes such as galvanic replacement reactions (GRR), can initiate unique out-of-equilibrium thermodynamics and kinetics at the plasma–liquid interface. Such reaction pathways can generate novel nanostructures or, nanocomposites with tailored morphologies, compositions and metastable structures, heretofore not observed while being potentially promising for catalytic performances. To the best of our knowledge, few works have investigated structure–property relations (specifically for catalytic studies) in nanostructured materials emerging from complex plasma interactions/chemical reactions during LASiS.

In our effort to address the aforementioned key challenges in the facile and yet, chemically clean synthesis of bi-functional electrocatalysts, we report for the first time pulsed LASiS in tandem with galvanic replacement reactions (GRR) as an alternative cheap, one-step, one-pot route to synthesize nanocomposites (NCs) that exhibit superior ORR and OER catalytic activities with high stability. Specifically, we synthesize NCs comprised of PtCo nanoalloy embedded in CoO_x matrices by using our in-house designed multi-functional tandem LASiS–GRR technique. In turn, the structure–property characteristics of the as-synthesized PtCo/CoO_x NCs were investigated, specifically in terms of their ORR and OER catalytic activities.

2. Experimental

2.1. Synthesis of Co_3O_4 NPs and PtCo/CoO_x NCs

LASiS on bulk Co target was carried out to generate CoO/Co_3O_4 NPs, based on our earlier work [58], under different laser fluences (high fluence, HF: ~60 J/cm^2 and low fluence, LF: ~1 J/cm^2). Co pellets were bought from Kurt J. Lesker (99.95% purity, 1/4″ diameter × 1/4″ height) and Potassium tetrachloroplatinate(II) (K_2PtCl_4) (>99.9%) were bought from Sigma–Aldrich. All LASiS–GRR experiments were carried out in an in-house built cell equipped with facilities for simultaneous injection of metal salt solutions, temperature control as well as ultrasonication, as depicted in the supporting information (Fig. S1) and discussed in details in our earlier work [58]. For LASiS on Co, the Co pellets were covered by 35 ml of de-ionized water (DI-water; purity = 99.9%; conductivity = 18.2 MΩ/cm at 25 °C) and ablated for 15 min.

For the synthesis of PtCo/CoO_x NCs via tandem LASiS-GRR technique, different amounts of K_2PtCl_4 salts were dissolved in 40 ml of DI-water to produce four different concentrations of K_2PtCl_4 solutions, namely 25, 60, 120 and 250 mg/l. Thereafter, each of the freshly prepared K_2PtCl_4 solution was transferred into the LASiS cell through the injection unit. The Co pellet was then ablated in those K_2PtCl_4 solutions for 20 min. The obtained colloidal solutions were aged for three days under ambient temperature and pressure conditions. Then, the samples were centrifuged at 5000 rpm for 15 min and decanted after washing with DI-water for two times. Both LASiS and tandem LASiS–GRR experiments were carried out at room temperature with simultaneous ultrasonication. The Co tar-
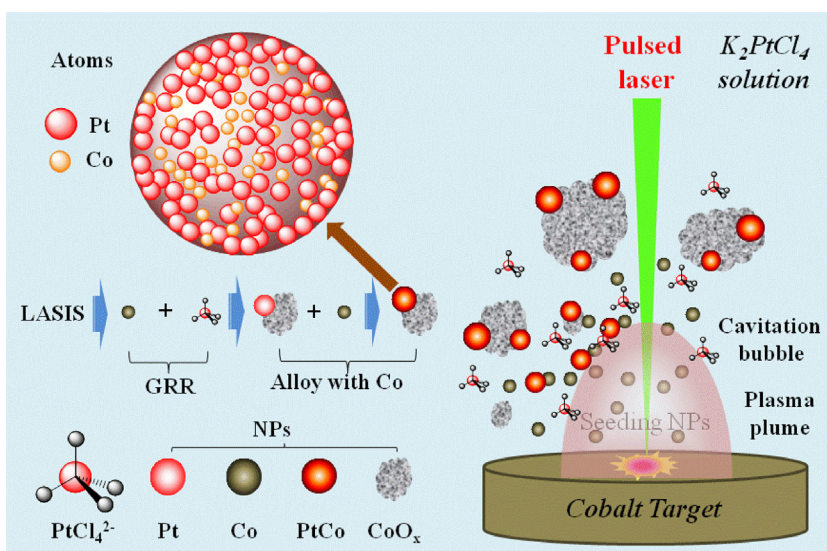
Fig. 1. Schematic representation of the tandem LASiS-GRR technique that synthesize $PtCo/CoO_x$ nanocomposites (NCs).

get was rotated by a stepper motor at a uniform speed of 0.3 rpm during ablation.

2.2. Characterization

A Zeiss Libra 200MC monochromated transmission electron microscope (TEM) was used with an accelerating voltage of 200 kV for regular TEM, selected area diffraction (SAED), high resolution image (HRTEM) and energy dispersive X-ray spectrometer (EDX) analysis. Inductively coupled plasma optical emission spectroscopy (ICP-OES) (PerkinElmer, Optima 4300 DV) was used to measure the concentration for both Pt and Co NPs. Standard cobalt dichloride solution ($\geq$99%) and K_2PtCl_4 solution (>99.9%) were used for calibration. X-ray diffraction (XRD) was carried out on a Phillips X'Pert-Pro diffractometer equipped with a Cu Ka source at 45 kV and 40 mA.

2.3. Electrochemical tests

The rotating disk electrode (RDE) setup was bought from Pine instrument company, LLC. A conventional, three-compartment electrochemical cell comprising of a saturated double junction Ag/AgCl electrode as the reference electrode, a glassy carbon RDE with diameter of 5 mm as the working electrode, and a platinum coil as the counter electrode. All electrochemistry (EC) tests were carried out at room temperature in 1.0 M KOH solution with the reference electrode calibrated in response to the reversible hydrogen electrode (RHE). 30% Pt/C from BASF was used as the standard catalyst for comparison. For ORR tests, synthesized NPs were first mixed with Vulcan XC-72 carbon black (CB) powder (particle size 20–40 nm, procured from Cabot Company) in aqueous solution with a weight ratio of 1:4 (NP:CB). After 2 h of ultrasonication, the slurry was stirred for 24 h and then, completely dried in vacuum at 80 °C. Thereafter, the catalyst ink was prepared by suspending 2 mg of the dried mixture in 0.5 ml methanol and 25 μl of 5 wt% Nafion solution (Sigma–Aldrich, density 0.874 g/mL) via 30 mins of ultrasonication. For preparing the working electrode, 6 μL of the prepared catalyst ink was coated on the RDE where the NP loading density was calculated to be 24.5 μg/cm². As for the OER tests, synthesized NPs were deposited on the GCE directly by vacuum drying at room temperature, with a deposition density calculated as 2 μg/cm² for all the catalysts. Linear sweep voltammogram (LSV) for ORR and OER were conducted on the RDE set-up by sweeping

the potential from +0.3 to +1.1 V (ORR) and +1.1 to +1.7 V (OER) respectively. For all the experiments, stable voltammogram curves were recorded after scanning for 15 cycles in the corresponding potential regions. The dynamics of the electron transfer process in ORR were analyzed through the rotating disk voltammetry (RDV) at different speeds (ranging between 400 and 2200 rpm) based on the Koutecky–Levich (KL) equation:

$$\frac{1}{J} = \frac{1}{J_K} + \frac{1}{J_L} = \frac{1}{J_K} + \frac{1}{B\omega^{1/2}}$$

$$J_K = nFkC_0 \quad ; B = 0.62nFC_0D_0^{2/3}\nu^{-1/6}$$

where J, J_K and J_L are the measured, kinetic and diffusion limiting current densities respectively, n is the electron transfer number, F is the Faraday constant (96 485 C mol^{-1}), C_0 and D_0 are the dissolved O_2 concentration the O_2 diffusion coefficient in the electrolyte respectively, ν is the electrode rotation rate in rpm. Tafel plots are generated using the kinetic current J_K as determined from:

$$J_K = \frac{J \times J_L}{J_L - J}$$

3. Results and discussion

### 3.1. Mechanistic picture of LASiS-GRR

In the current tandem LASiS–GRR technique, the galvanic replacement reaction (GRR) between K_2PtCl_4 and Co occurs in the above-mentioned system based on the respective redox potentials for Co/Co^{2+} (-0.28 V vs. SHE) and $PtCl_4^{2-}/Pt$ (0.76 V vs. SHE) as:

$$PtCl_4^{2-} + Co \rightarrow Pt + Co^{2+}$$
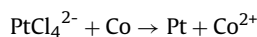
However, it is obvious that further oxidation of Co^{2+} to Co^{3+} cannot be initiated by the simultaneous reduction of solution phase Pt^{2+} ions since the mid-point potential for Co^{2+}/Co^{3+} is much higher (1.82 V vs. SHE). Theoretically, the displacement reaction can occur between $PtCl_4^{2-}$ and any metal with redox potential <0.76 V vs. SHE (for $PtCl_4^{2-}/Pt$).

Fig. 1 shows the schematic for the reaction pathways during LASiS–GRR that lead to the NC formation. Pulsed laser beam creates a liquid confined plasma plume with extremely high temperature
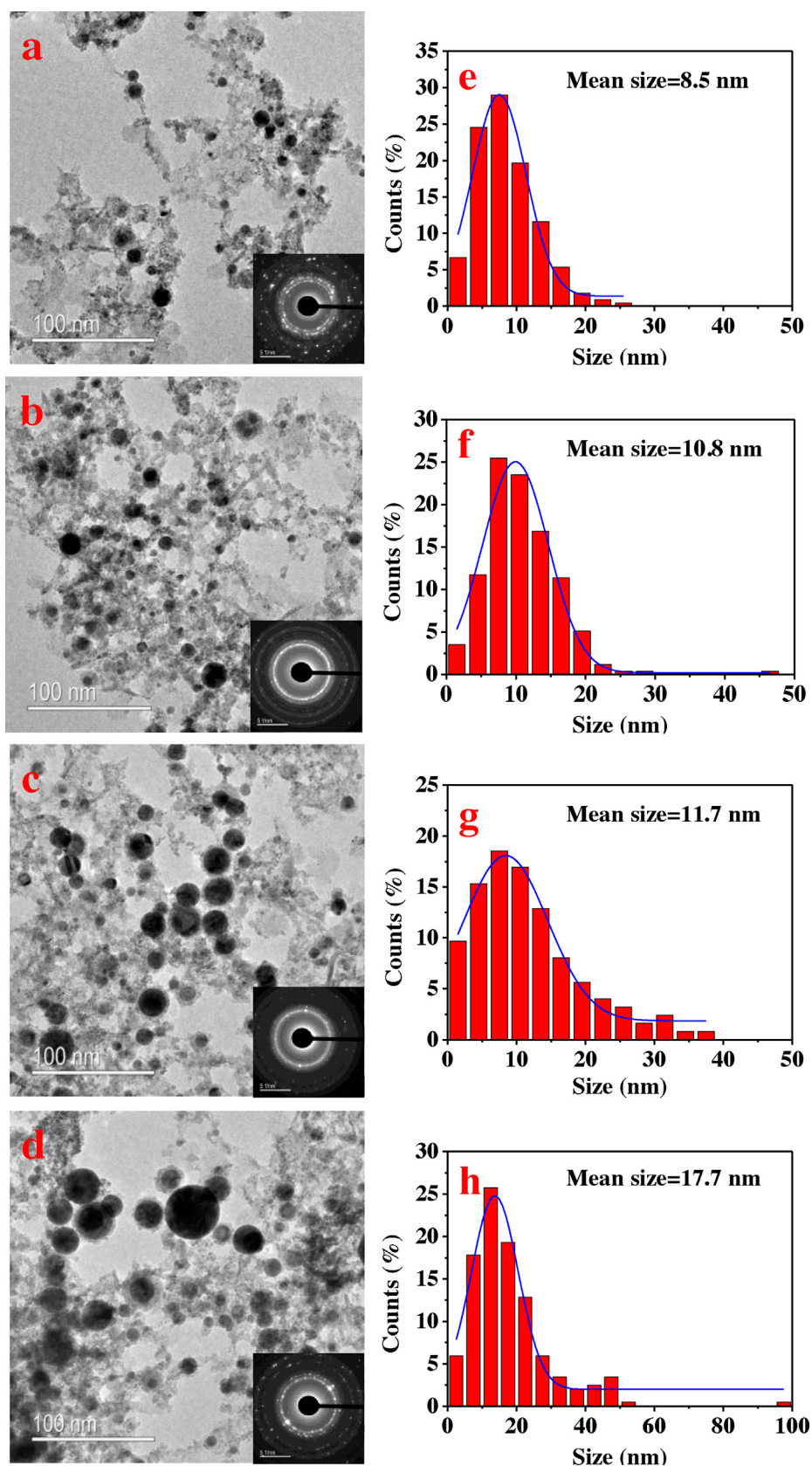
Fig. 2. (a–d) TEM images (Magnification: 80 K) along with the corresponding SAED patterns (inset) for the PtCo/CoO$_x$ NCs synthesized by LASIS–GRR using different Pt:Co atomic ratios of: (a) 1:9 (PtCo-1); (b) 1:4 (PtCo-2); (c) 1:2 (PtCo-3); (d) 1:1 (PtCo-4). The scale bar in for SAED patterns is 5 (1/nm); (e–h) Corresponding size distributions for dark colored PtCo alloyed NPs in a–d.
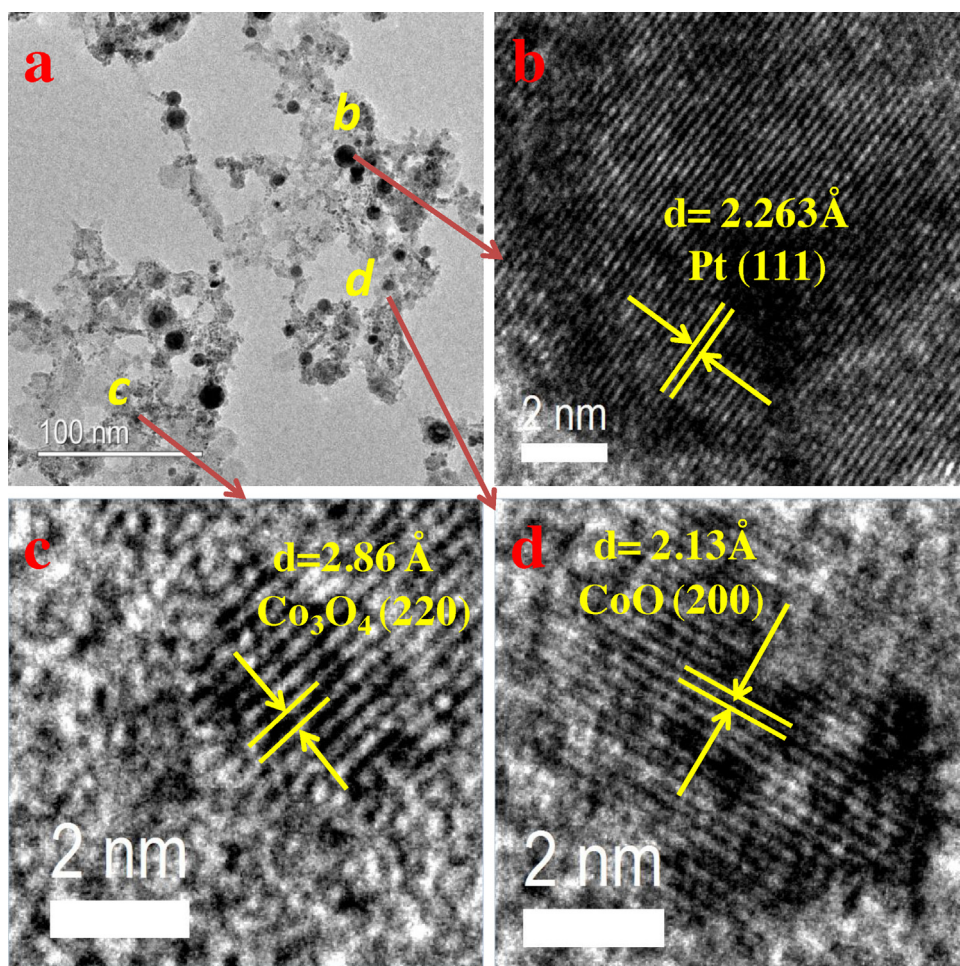
Fig. 3. (a) Representative TEM image of PtCo-1 sample with the corresponding positions marked (b–d) indicating the lattice fringes in the HRTEM images for: (b) Pt, (c) Co_3O_4, and (d) CoO respectively.
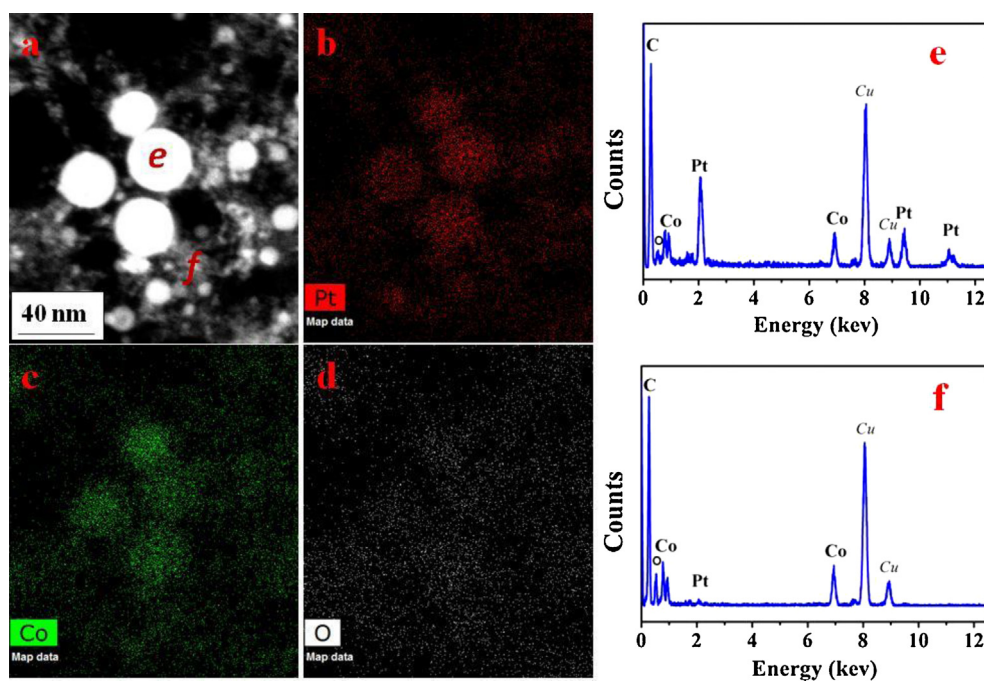
Fig. 4. EDX results for PtCo-3 sample along with: (a) HAADF image, and elemental mappings for (b) Pt, (c) Co and (d) O respectively; (e, f) Corresponding EDX spectra at the positions marked in a. (Cu and C signals are from the TEM carbon film with copper grids).
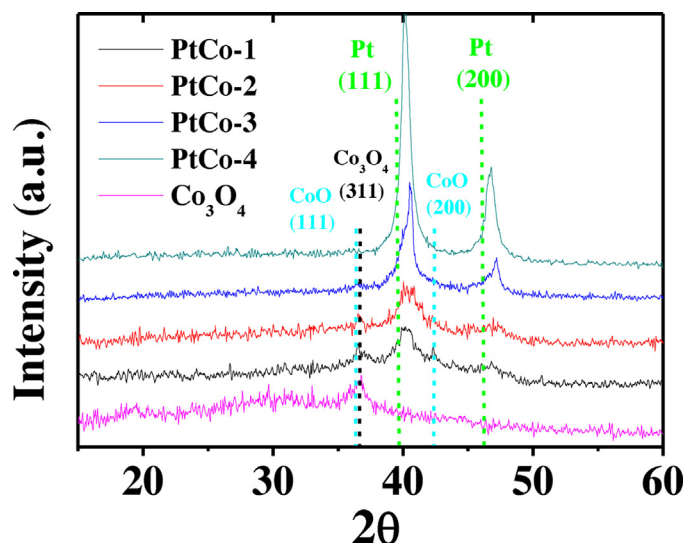
Fig. 5. Comparison of XRD patterns for PtCo/CoO$_x$ nanocomposites with different Pt:Co ratios along with standard peak positions for Co$_3$O$_4$, CoO and Pt indicated by black, blue and green vertical lines respectively.

and pressure on the Co surface that results in thermal vaporization of the metal target. Large amount of seeding NPs then start to form inside an oscillating cavitation bubble resulting from the expanding plasma plume. Thereafter, the seeding NPs undergo collisional quenching and redox reactions with the solution phase ionic species at the bubble–liquid interface upon the bubbles collapse. However, only part of those seeding Co NPs can go through GRR with K$_2$PtCl$_4$ due to the high local concentration but limited reaction rate, thereby leaving the rest of them either coalesce (alloy) with reduced Pt or get oxidized by the solution phase O$_2$/H$^+$. The newly formed intermetallic PtCo NPs then continue to coalesce with each other into large spherical NPs that are partially embedded into the CoO$_x$ matrices.

3.2. Structure and composition analysis for the PtCo/CoO$_x$ NCs

In our recent work explaining the mechanism of LASiS, it was shown that LASiS on bulk cobalt produces meta-stable CoO, which further oxidizes rapidly into stable Co$_3$O$_4$ in the aqueous solution [58]. In the current work, we carried out LASiS on cobalt with four different initial K$_2$PtCl$_4$ concentrations (i.e., 25 mg/l, 60 mg/l, 120 mg/l and 250 mg/l) to produce four different NP colloidal samples labeled here onwards as PtCo-1, PtCo-2, PtCo-3 and PtCo-4 respectively. The corresponding Pt and Co NP concentrations in each of the samples, as revealed from ICP-OES measurements, are summarized in Table 1. The results indicate that ~60–70% of the precursor Pt salt is transformed into Pt NPs upon ablation at 60 J/cm^2 fluence for 30 min. The Pt:Co molar ratios was calculated to be 1:9, 1:4, 1:2 and 1:1 for PtCo-1 to PtCo-4 respectively. The unreacted residual K$_2$PtCl$_4$ as well as any excess KCl formed are washed away during the centrifugation step. This is also confirmed by the TEM images, as shown in Fig. 2(a–d), indicating that mainly two types of nanostructures are found in all four samples, namely individual spherical NPs (darker contrast) embedded in a large amount of highly porous "sponge-shaped" nanostructures (lighter contrast). These structures are expected to be CoO$_x$ (lighter) and Pt and/or PtCo intermetallic (darker) NPs respectively, where the different contrasts in the transmitted electron intensities are due to their different mass to charge ratios. The size distributions for the darker spherical Pt-based NPs (which are later revealed to be Pt–Co nanoalloys) are shown in Fig. 2e–h, where the mean sizes increase from 8.5 nm to 17.7 nm with the increase of the Pt:Co ratios. This

is ascribed to the enhanced coalescence due to increased concentrations of Pt NPs. The existence of Pt and CoO$_x$ NCs are further confirmed by the identification of their respective crystalline structures in the SAED patterns (shown in the insets of Fig. 2a–d) along with calculated d-spacing values (provided in the supporting information in Table S1). However, in our earlier work [58] with LASiS on bulk Co (without any K$_2$PtCl$_4$), we had shown that initially formed metastable CoO upon three days of ageing underwent complete oxidization into Co$_3$O$_4$ by the solution phase O$_2$ and H$^+$. In contrast, the present study indicates that LASiS on Co in the presence of K$_2$PtCl$_4$ salt solution, when exposed to the identical ageing process, results in both Co$_3$O$_4$ and CoO nanostructures coexisting in the final products. This is possibly due to the highly non-equilibrium processes where the seeding Co NPs emerging from the cavitation bubble undergo ultra-fast quenching and reactions with the solution phase metal salt ions at the liquid front. Thus, during ablation in the aqueous solution with K$_2$PtCl$_4$ salts, a large portion of Co is converted to CoO through galvanic replacement reaction (GRR) rather than direct oxidation, since the redox potential for Pt^{2+} → Pt^0 (0.76 V vs. SHE) is even higher than O$_2$ → O^{2-} (0.4 V vs. SHE). The relatively higher stability of these CoO NPs could possibly be due to this inherently different formation mechanism. As a result, it is difficult for the CoO NPs to further get oxidized into Co$_3$O$_4$ or the oxidation rate is much slower. In addition, high resolution TEM images (HRTEM) indicate the three different areas marked as b–d in Fig. 3a that correspond to Pt (111) (d = 2.26 Å), Co$_3$O$_4$ (220) (d = 2.86 Å) and CoO (200) (d = 2.13 Å) exposed to the surface, as shown in Fig. 3b–d respectively. Lastly, control experiments were also carried out for laser irradiation on the K$_2$PtCl$_4$ solution only (without any Co target), in which case no Pt NPs are formed (Fig. S7), confirming that the formation of Pt NPs is largely due to the galvanic replacement reactions (GRR).

In order to further investigate the elemental composition and distribution in the products, EDX tests were carried out for the STEM mode images. The results from the high-angle annular dark-field (HAADF) image, as shown in Fig. 4a specifically for the PtCo-3 sample, reveal the corresponding elemental mappings for Pt, Co and O, (Fig. 4b–d respectively). These images show that Pt is mainly distributed in the bright spherical NPs in the HAADF image (i.e., the four large NPs at the center). In contrast, Co is mostly distributed in the background gray areas although its presence is strongly noted inside the brighter NPs (see Fig. 4c), while O is found to be uni-
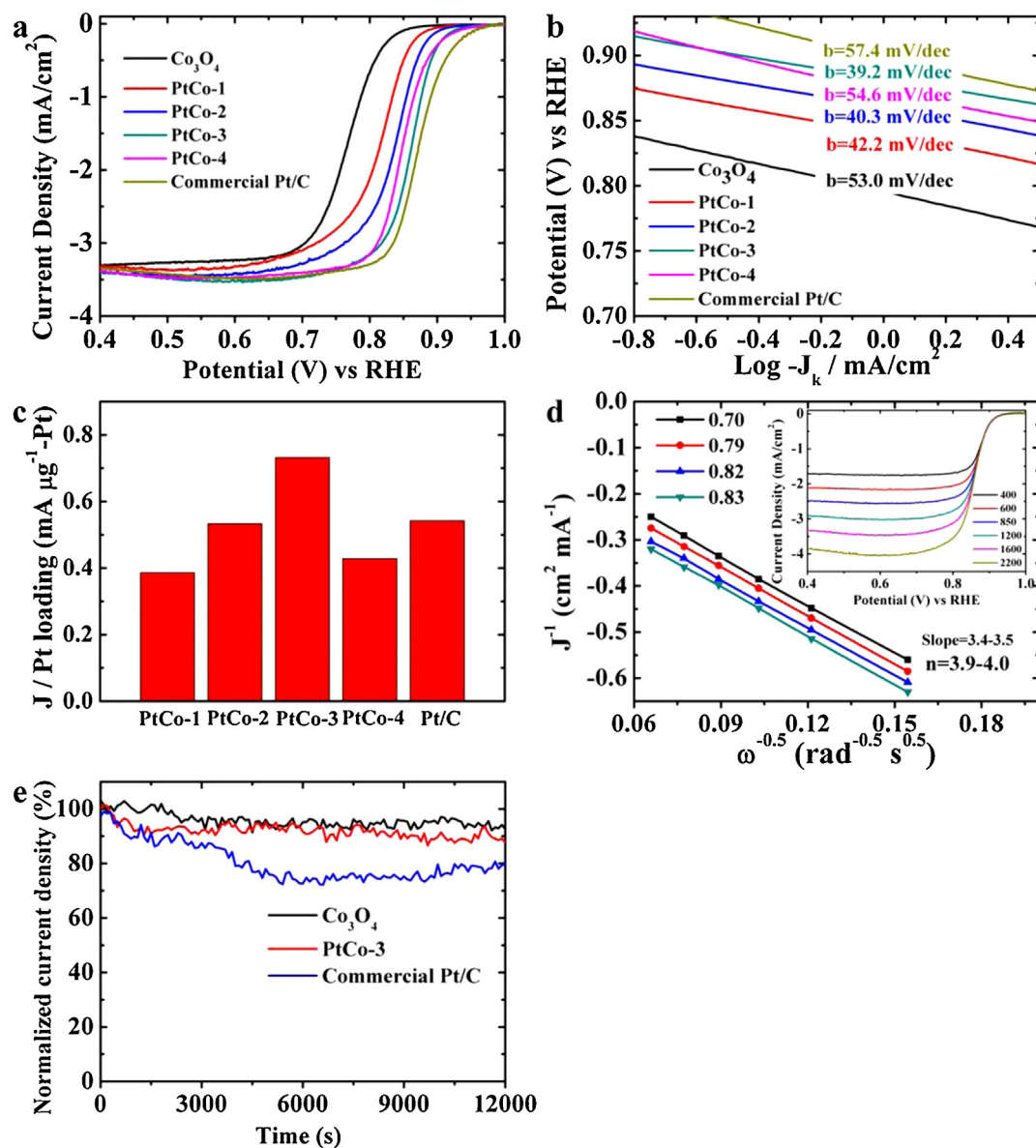
Fig. 6. Electrochemistry data for as-synthesized Co_3O_4 NPs and PtCo/CoO$_x$ NCs compared to standard Pt/C samples using: (a) Linear sweep voltammograms for ORR analysis in 1 M KOH electrolyte saturated with dissolved O_2 at 1600 rpm and scan rate of 5 mV/s; (b) Tafel plots from a; (c) Comparison of mass activities per unit Pt mass loading at 0.85 V vs. RHE; (d) Koutecky–Levich plots from rotating disk voltammogram (RDV) data (shown in inset) for PtCo-3 at different potentials (0.70–0.83 V) indicate four electron transport process for ORR; (e) Stability comparison for Co_3O_4, PtCo-3 and standard Pt/C through chronoamperometry (CA) tests.

Table 1
Pt and Co concentrations from ICP-OES measurements for various PtCo/CoO$_x$ NCs synthesized by LASiS–GRR at different initial K_2PtCl_4 salt concentrations.

	Initial K_2PtCl_4 conc. (mg/l)	Pt conc. (mg/l)	Co conc. (mg/l)	Molar Pt/Co ratio
PtCo-1	25	7.3	20	1:9
PtCo-2	60	19	23	1:4
PtCo-3	120	42	25	1:2
PtCo-4	250	81	25	1:1

Table 2
Calculated alloyed Pt:Co ratio from XRD results in Fig. 5.

Sample	2θ (°)	Lattice constant (Å)	Pt:Co
PtCo-1	40.2	3.88	8.6:1
PtCo-2	40.3	3.87	6.7:1
PtCo-3	40.5	3.85	4.6:1
PtCo-4	40.1	3.89	11.5:1

formly distributed in the whole image. Furthermore, detailed EDX spectra in Fig. 4e and f which correspond to the areas marked e and f respectively in Fig. 4a indicate strong Pt and Co peaks along with weak O peak inside the bright spherical particle (Fig. 4e). In comparison, Fig. 4f indicates negligible Pt peak along with a relatively strong O peak in the background areas. It is noted here that the Cu and C signals in the spectra are from the TEM carbon film with copper grids. The absence of any other detectable elements in the EDX data indicates that all the residual chemicals such as K_2PtCl_4 and KCl have been washed away by the centrifuging process. The aforementioned results for the elemental mappings of Pt, Co and O in Fig. 4b, c and d, along with the EDX spectral intensities in Fig. 4e and f, clearly suggest the formation of PtCo nanoalloy inside the bright spherical NPs (marked as the areas e in Fig. 4a). This also validates our earlier assumption that the as-synthesized nanocomposites are made of PtCo nanoalloy (the brighter NPs) embedded in the CoO/Co_3O_4 matrices.

To corroborate the above mentioned results, Fig. 5 summarizes the XRD data for all the PtCo/CoO$_x$ NCs dispersed in carbon black, where the sample from LASiS on Co (without the K_2PtCl_4 salt) displays the distinct Co_3O_4 (311) peak (PDF-#42-1467) at $2\theta = 36.9°$ but does not show any characteristic peak for CoO (PDF-#43-1004). In contrast, the PtCo-1 sample indicates a CoO (200) peak at $2\theta = 42.4°$ along with a minor peak at $2\theta = \sim36.6°$ which is assigned as an overlapped peak of CoO (111) ($2\theta = 36.5°$) and Co_3O_4 (311) ($2\theta = 36.9°$). These results further confirm our previous SAED data in Fig. 2.d that the CoO gets partially conserved in the PtCo/CoO$_x$ NCs that do not undergo further oxidation during the ageing process. Meanwhile, two distinct characteristic peaks are also observed for this sample at $2\theta = 40.2°$ and $2\theta = 46.7°$ that are assigned to the (111) and (200) peaks for PtCo alloy. Here, one needs to note that the 2θ values for standard Pt are 39.8° (111) and 46.2° (200) (PDF-#04-0802). The shift of these peaks to higher angles is attributed to the Pt alloying with Co that result in a shrunken lattice constant calculated to be ~3.88 Å as compared to 3.92 Å for standard Pt. Besides, Fig. 5 also reveals that the alloyed PtCo peaks quickly become dominant with the increase of Pt:Co ratio. Specifically, for the case of PtCo-3 and PtCo-4 (Pt–Co ratio equals to 1:2 and 1:1), the CoO$_x$ peaks are barely discernable, which is ascribed to the much higher crystallinity and hence, the diffraction pattern intensity for Pt alloyed with Co as compared to that for CoO$_x$. It needs to be noted here that this phenomenon is also supported by the previous SAED patterns in the insets of Fig. 2a–d. The alloyed Pt:Co ratios from PtCo-1 to PtCo-4 are estimated to be 8.6:1, 6.7:1 and 4.6:1 and 11.5:1 respectively according to the Vegard's law [7], as summarized in Table 2. As also described earlier in Fig. 1, the seeding Co NPs from the cavitation bubble go through two competing reactions, namely, either GRR with Pt^{2+} or oxidation by solution phase O_2 and H^+. When the initial K_2PtCl_4 concentration is low, a large portion of Co will react with solution phase O_2/H^+, thereby leaving few available seeding Co NPs to alloy with Pt formed via GRR mediated reduction by Co. Hence, the Co:Pt ratio in the PtCo alloys rises at first with increasing initial K_2PtCl_4 concentrations in the solution. However, beyond a critical value, further increase of Pt^{2+} ion concentrations leads to oxidation of Co atoms in the initially formed PtCo alloy. Such a de-alloying process will reduce the amount of alloyed Co in the PtCo nanoalloys, and has already been reported by some other works [62].

3.3. Investigation of ORR/OER catalytic activities

The catalytic activities for both pure Co_3O_4 NPs and PtCo/Co_3O_4 NCs were tested with the aid of the rotating disk electrode (RDE) measurement in O_2-saturated 1 M KOH solution, as shown in Fig. 6. In order to overcome the electronic conductivity limitations and increase the catalytic surface area for ORR experiments, all the syn-

thesized NCs were dispersed in CB (Vulcan XC-72R, weight ratio NP:CB = 1:4). It needs to be mentioned that linear sweep voltammograms (LSV) on pure Co_3O_4 NPs generated from high fluence (HF, 60 J/cm^2) and low fluence (LF, 1 J/cm^2) LASiS in our earlier work (Supplementary Fig. S8) indicated that half-wave potentials and diffusion limiting currents for HF Co_3O_4 samples are better than those for LF Co_3O_4 samples (i.e., 770 mV and 3.25 mA/cm^2 vs. 740 mV and 2.75 mA/cm^2 for HF vs. LF samples respectively). This is attributed to the uniform sizes and spherical shapes of HF Co_3O_4 NPs obtained from the explosive boiling mechanism of LASiS at high laser energy. Hence, the choice for all catalytic studies presented in the present article are for the Co_3O_4 and PtCo/CoO$_x$ samples synthesized at HF (60 J/cm^2) conditions. We also noted that the measured ORR catalytic activities for our Co_3O_4 NPs itself compared extremely well with those observed by other peer works [8,15,22,23]. We believe that the clean, one-step synthesis process for LASiS plays a role here in generating these NPs devoid of any additional chemicals (surfactants, reducing agents, etc.) that can retard or poison their catalytic activities. Fig. 6a compares the ORR catalytic performance for each of the catalyst samples under study through the LSV test. The results indicate a remarkable improvement for the ORR activities with the increase of Pt to Co ratio from 1:9 (PtCo-1) to 1:2 (PtCo-3). Specifically, the half-wave potential for the PtCo-3 sample is improved to 860 mV, which is almost comparable to the corresponding values for standard Pt/C samples (870 mV). The ORR overpotential for this sample is calculated to be 370 mV based on the standard potential for reduction of oxygen to water being 1.23 V. However, as the Pt:Co ratio further increases to 1:1 for PtCo-4, the half-wave potential slightly reduces to 850 mV, with the overpotential calculated to be 380 mV. Besides, Fig. 6b compares the Tafel plots for the abovementioned samples generated from Fig. 6a over the low overpotential regions. The measured Tafel slope values are 53.0, 42.2, 40.3, 39.2 and 54.6 mV/dec respectively as compared to ~66.2 mV/dec for standard Pt/C samples, thereby indicating higher charge transfer coefficients for the as-synthesized catalysts. Fig. 6c further compares the mass activities per unit Pt loading amount at 0.85 V vs. RHE for the PtCo/CoO$_x$ NCs studied. The results indicate a much higher mass activity for PtCo-3 sample (0.73 mA μg^{-1} Pt) than the commercial Pt/C (0.54 mA μg^{-1} Pt). The other three samples (PtCo-1, PtCo-2 and PtCo-4) demonstrate lower but comparable mass activities, although the PtCo-4 sample with an increased amount of Pt indicates a marked drop in the ORR activity. The excellent ORR activities for these materials are mainly attributed to the following reasons. Firstly, the formation of alloyed PtCo nanostructures shrinks the Pt lattice constants and decreases the effective sites for OH$^-$ adsorption. Added to that, it enhances the Pt$-$O bonding due to higher 5d orbital vacancies in its electronic structure that promotes the donation of π electrons from O_2 to Pt [11,21]. Hence, the sites on the PtCo alloy NPs (known for their ORR activities) preferentially promote both O_2 adsorption and OH$^-$ desorption, both benefit the ORR efficiency. Secondly, the NC of the metal-transition metal oxide (NM-TMO) system further benefits the ORR process by providing a synergic "spill-over" effect [42,46]. Specifically, the OH$^-$ reduced from O_2 is readily desorbed from the active PtCo sites and transferred to the sponge-shaped CoO$_x$ sites which are less active according to their respective M$-$O bonding strength and intermolecular affinities. Thus, the best ORR activity is promoted by the PtCo-3 catalyst with optimal Pt content (33.3 molar%, 62.3 wt.%) that leads to higher degree of Pt-Co alloy formation (confirmed by Fig. 5 and Table 2) with more lattice shrinkage and appropriate sizes (mean size = 11.7 nm), as well as by the balanced PtCo to CoO$_x$ ratio that potentially maximizes the synergic "spill-over" effects.

The dynamics of the electron transfer process during ORR activities of the aforementioned catalysts are analyzed using the Koutecky–Levich (KL) equation for rotating disk voltammetry
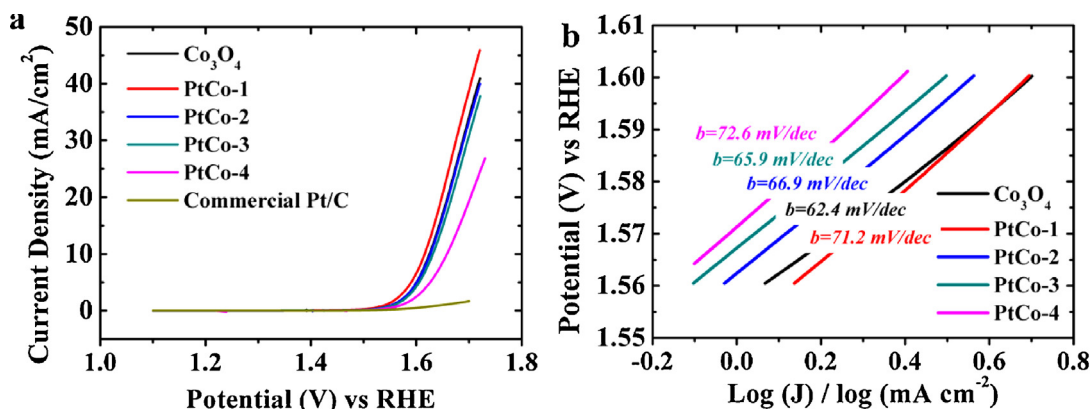
Fig. 7. (a) Linear sweep voltammograms for OER analysis on PtCo/CoO$_x$ NCs compared to those for Co$_3$O$_4$ NPs and standard Pt/C samples; (b) Corresponding Tafel plots in the potential range of 1.55–1.60 V.
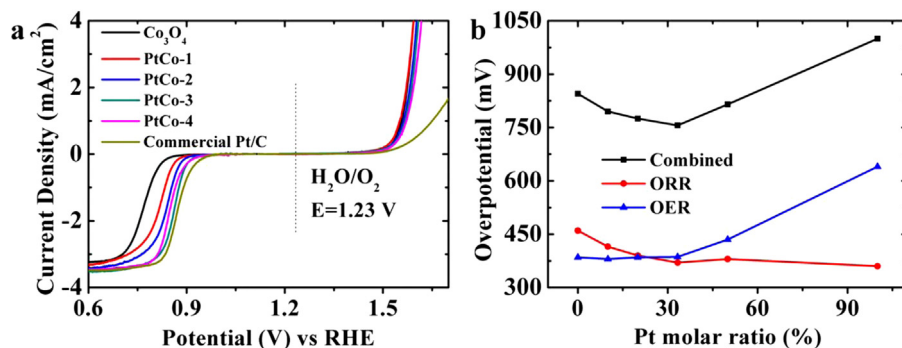

Fig. 8. (a) Comparison of bifunctional catalytic activities for both OER and ORR through Linear sweep voltammogram (LSV); (b) Evolution of ORR, OER and combined overpotentials for catalytic samples understudy with the increase of Pt molar ratio.

Fig. 9. Schematic illustrating the mechanism ofthe "spill-over effect".

(RDV) measurements carried out at different speeds. Fig. 6d shows the slopes for the KL plots generated from rotation-rate dependent current–potential curves (inset in Fig. 6d) for the PtCo-3 NCs in the range of 0.70–0.83 V. The slopes estimate the number of electrons transferred (n) to be 3.9–4.0, thereby indicating an ideal four-electron transport process for the ORR activity. (Detailed RDV data and KL plots for PtCo-1, PtCo-2 and PtCo-4 NCs are provided in Fig. S9 in the supporting information that indicate the corresponding electron transfer numbers to be 3.8–4.0 for all of them.

In addition to the good ORR catalytic activities, chronoamperometric (CA) measurements also reveal excellent stabilities for the PtCo-3 NC samples. Fig. 6e compares the normalized current den-

sity (%) at the corresponding half-wave potentials for the Co$_3$O$_4$, PtCo-3, and standard Pt/C samples. As can be seen from the results, the ORR current densities decay by less than 15% over 12,000s of continuous operation for both the Co$_3$O$_4$ and PtCo-3 samples. In contrast, the standard Pt/C sample indicates a ca. 28% current density reduction over the same period of time. The decay in the catalytic activities of standard Pt/C samples is attributed to its surface oxidation as well as particle dissolution and aggregation in the alkaline electrolyte [18], which hardly occur for the metal oxides (Co$_3$O$_4$/CoO). In fact, in the case of the PtCo/CoO$_x$ NCs, the existence of the sponge-shaped CoO$_x$ serve as a matrix material that protects the PtCo alloyed NPs from aggregation or dissolution. Meanwhile, the alloyed PtCo structure also helps to slow down the oxidation of Pt due to the much higher electron negativity of Co.

Finally, the OER catalytic activities for the PtCo NC samples are investigated by comparing with the results for pure Co$_3$O$_4$ and standard Pt/C samples, as shown in Fig. 7. For comparing the OER overpotentials, all potential measurements were carried out with 10 mA/cm^2 as the metrics due to its relevance to solar fuel characterizations [6]. The results reveal that, with an overpotential of 385 mV (Fig. 7a) and a measured Tafel slope of 62.4 mV/dec, the LASiS generated Co$_3$O$_4$ itself is comparable or, even better than other reported OER catalysts [6,8,13,38,39,44]. As expected, the standard Pt/C sample shows the worst OER activities (with an overpotential of ∼640 mV). As also mentioned earlier, the high OER activity for our Co$_3$O$_4$ NPs is attributed to the clean synthesis route of LASiS that produces the sponge-like nanostructures with enhanced surface area that do not have any surface contamination from unwanted chemicals during the preparation. But, the most significant observation from Fig. 7a is that the PtCo-1 sample exhibits an even smaller OER overpotential (380 mV) than the
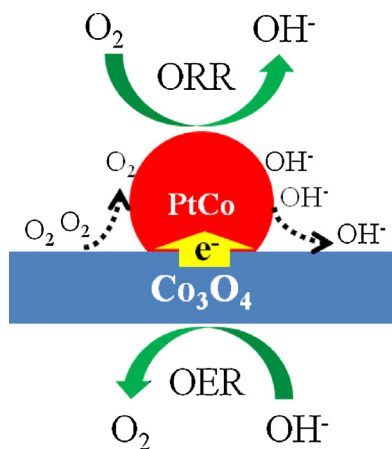
Co_3O_4 sample that is typically well-known for OER activities. In fact, the overpotentials for PtCo-2 and PtCo-3 are also comparable ($\sim$385 and 386 mV respectively), indicating that these PtCo/CoO$_x$ NCs exhibit good OER catalytic activities as well. Here we also note that the PtCo-4 sample displays a relatively poorer activity (overpotential of $\sim$ 435 mV) that could be possibly due to the scarcity of CoO$_x$ in the NC catalyst. It is also noted here though that Tafel slopes for the PtCo NCs are slightly larger ($\sim$71–72 mV/dec for PtCo-1 and PtCo-4 whereas, $\sim$66–67 mV/dec for PtCo-2 and 3) as compared to those for pure Co_3O_4 ($\sim$ 62.4 mV/dec) as seen in Fig. 7b. The enhanced OER performance can also be attributed to the aforementioned synergic "spillover" effect for specific NM-TMO systems, where the produced O_2 is desorbed from active CoO$_x$ surfaces and transferred to relatively inert PtCo nanoalloy sites with higher O_2 affinity. For better understanding, a schematic in Fig. 9 illustrates the detailed mechanistic picture behind the synergic "spill-over" effects responsible for the site-specific adsorption/desorption of the desired species to promote the bifunctonal catalytic performances in the aforementioned NCs. For both ORR and OER, the PtCo sites and CoO$_x$ matrices provide synergic support for each other wherein each of the sites provides refuge for the undesirable species from the other sites, thereby promoting both the reactions.

The combined overpotentials for PtCo-1 to PtCo-4 are calculated to be 795, 775, 756, and 815 mV respectively, which remarkably outperform the overpotentials for either Co_3O_4 or the commercial Pt/C (i.e., 845 mV for Co_3O_4 and 1000 mV for commercial Pt/C), as shown in Fig. 8. a and b as well as reported in Table S2. These results indicate that the synthesized PtCo NCs exhibit superior bifunctional catalytic performances for both ORR and OER processes, especially for the PtCo-3 sample with an optimal Pt amount (33.3 M%, 62.3 wt.%). Overall, we attribute the excellent bifunctional catalytic properties of the PtCo/CoO$_x$ NCs to the unique heteronanostructuring of alloyed PtCo NPs embedded in the sponge-shaped CoO$_x$ matrices which, while contributing to the enhanced ORR and OER behaviors due to the synergic "spillover" effects, prevent the PtCo NPs from aggregation and dissolution in the alkaline media.

4. Conclusions

We presented a novel one-pot, one-step, "green" synthesis route that combines laser ablation synthesis in solution in tandem with galvanic replacement reactions (tandem LASiS–GRR) to manufacture complex PtCo/CoO$_x$ nanocomposites (NCs) with outstanding ORR and OER catalytic activities. The transformative concept here is the ability to synthesize such complex heteronanostructures in one step without the need for any harsh chemical reagents and/or, surfactants. This is made possible by the out-of-equilibrium thermodynamic conditions emerging from extreme physicochemical conditions of high energy LASiS operating in tandem with chemical reduction processes (GRR in this case). The synthesized PtCo NCs exhibited excellent yet, stable catalytic activities for both oxygen reduction reactions (ORR) and oxygen evolution reactions (OER) in alkaline media. Specifically, we reported a combined overpotential of 756 mV vs. RHE for the PtCo-3 NC (33.3 M%, 62.3 wt.%), which is the highest value ever reported using carbon black as the supporting material. This excellent bifunctional activity is attributed to the structural and electronic properties of PtCo nanoalloy that promote oxygen adsorption, as well as to the sponge-shaped CoO$_x$ matrices in which the PtCo NPs are embedded that bring about the synergic "spillover" effects to facilitate both ORR and OER activities. Added to this, the CoO$_x$ matrix also prevents the PtCo NPs from aggregation and dissolution in alkaline electrolytes. Encouraged by the current results, we have work in progress to extend the aforementioned clean yet, facile synthesis routes for the future design of various complex intermetallic NCs in a rapid and cost-effective fashion.

Appendix A. Supplementary data

Supplementary data associated with this article can be found, in the online version, at http://dx.doi.org/10.1016/j.apcatb.2015.09.035.

References

[1] H.B. Gray, Powering the planet with solar fuel, Nat. Chem. 1 (2009) 112, http://dx.doi.org/10.1038/nchem.206.
[2] H.A. Gasteiger, N.M. Marković, Chemistry. Just a dream—or future reality? Science 324 (2009) 48–49, http://dx.doi.org/10.1126/science.1172083.
[3] S. Park, Y. Shao, J. Liu, Y. Wanu, Oxygen electrocatalysts for water electrolyzers and reversible fuel cells: status and perspective, Energy Environ. Sci. 5 (2012) 9331, http://dx.doi.org/10.1039/c2ee22554a.
[4] Y. Liang, Y. Li, H. Wang, J. Zhou, J. Wang, T. Regier, et al., Co_3O_4 nanocrystals on graphene as a synergistic catalyst for oxygen reduction reaction, Nat. Mater. 10 (2011) 780–786, http://dx.doi.org/10.1038/nmat3087.
[5] X. Guo, W. Xu, S. Li, Y. Liu, X. Li, X. Qu, et al., Superstructures and their enhanced lithium-ion storage performances, Nanotechnology 23 (2012) 465401, http://dx.doi.org/10.1088/0957-4484/23/46/465401.
[6] Y. Gorlin, T.F. Jaramillo, A bifunctional nonprecious metal catalyst for oxygen reduction and water oxidation, J. Am. Chem. Soc. 132 (2010) 13612–13614, http://dx.doi.org/10.1021/ja104587v.
[7] N. Kristian, Y. Yu, J.M. Lee, X. Liu, X. Wang, Synthesis and characterization of Cocore-Ptshell electrocatalyst prepared by spontaneous replacement reaction for oxygen reduction reaction, Electrochim. Acta 56 (2010) 1000–1007, http://dx.doi.org/10.1016/j.electacta.2010.09.073.
[8] Y.J. Sa, K. Kwon, J.Y. Cheon, F. Kleitz, S.H. Joo, Ordered mesoporous Co_3O_4 spinels as stable, bifunctional, noble metal-free oxygen electrocatalysts, J. Mater. Chem. A 1 (2013) 9992, http://dx.doi.org/10.1039/c3ta11917c.
[9] R. Huo, W.-J. Jiang, S. Xu, F. Zhang, J.-S. Hu, Co/CoO/CoFe2O4/G nanocomposites derived from layered double hydroxides towards mass production of efficient Pt-free electrocatalysts for oxygen reduction reaction, Nanoscale 6 (2014) 203–206, http://dx.doi.org/10.1039/c3nr05352k.
[10] R. Lin, C. Cao, T. Zhao, Z. Huang, B. Li, A. Wieckowski, et al., Synthesis and application of core–shell Co@Pt/C electrocatalysts for proton exchange membrane fuel cells, J. Power Sources 223 (2013) 190–198, http://dx.doi.org/10.1016/j.jpowsour.2012.09.073.
[11] D. Wang, H.L. Xin, R. Hovden, H. Wang, Y. Yu, D.A. Muller, et al., Structurally ordered intermetallic platinum–cobalt core–shell nanoparticles with enhanced activity and stability as oxygen reduction electrocatalysts, Nat. Mater. 12 (2012) 81–87, http://dx.doi.org/10.1038/nmat3458.
[12] J.W. Hong, S.W. Kang, B.S. Choi, D. Kim, S.W. Lee, S.W. Han, Controlled synthesis of Pd–Pt alloy hollow nanostructures with enhanced catalytic activities for oxygen reduction, ACS Nano 6 (2012) 2410–2419, http://dx.doi.org/10.1021/nn2046828.
[13] Q. Yin, J.M. Tan, C. Besson, Y.V. Geletii, D.G. Musaev, A.E. Kuznetsov, et al., A fast soluble carbon-free molecular water oxidation catalyst based on abundant metals, Science 328 (2010) 342–345, http://dx.doi.org/10.1126/science.1185372.
[14] M.W. Kanan, D.G. Nocera, In situ formation of an oxygen-evolving catalyst in neutral water containing phosphate and Co^{2+}, Science 321 (2008) 1072–1075, http://dx.doi.org/10.1126/science.1162018.
[15] Y. Liang, H. Wang, J. Zhou, Y. Li, J. Wang, T. Regier, et al., Covalent hybrid of spinel manganese-cobalt oxide and graphene as advanced oxygen reduction electrocatalysts, J. Am. Chem. Soc. 134 (2012) 3517–3523, http://dx.doi.org/10.1021/ja210924t.
[16] E. Yeager, Electrocatalysts for O_2 reduction, Electrochim. Acta 29 (1984) 1527–1537, http://dx.doi.org/10.1016/0013-4686(84)85006-9.
[17] J. Snyder, I. McCue, K. Livi, J. Erlebacher, Structure/processing/properties relationships in nanoporous nanoparticles as applied to catalysis of the cathodic oxygen reduction reaction, J. Am. Chem. Soc. 134 (2012) 8633–8645, http://dx.doi.org/10.1021/ja3019498.
[18] W. Jin, H. Du, S. Zheng, H. Xu, Y. Zhang, Comparison of the oxygen reduction reaction between NaOH and KOH solutions on a Pt electrode: the electrolyte-dependent effect, J. Phys. Chem. B 114 (2010) 6542–6548, http://dx.doi.org/10.1021/jp102367u.

[19] B. Dembinska, Synthesis and characterization of new non-platinum electrocatalysts for oxygen reduction Beata Dembinska, ECS Trans. 45 (2013) 77–88.

[20] A. Trunov, Analysis of oxygen reduction reaction pathways on Co_3O_4, $NiCo_2O_4$, Co_3O_4–Li_2O, NiO, NiO–Li_2O, Pt, and Au electrodes in alkaline medium, Electrochim. Acta 105 (2013) 506–513, http://dx.doi.org/10.1016/j.electacta.2013.05.028.

[21] R. Loukrakpam, S. Shan, V. Petkov, L. Yang, J. Luo, C.J. Zhong, Atomic ordering enhanced electrocatalytic activity of nanoalloys for oxygen reduction reaction, J. Phys. Chem. C 117 (2013) 20715–20721, http://dx.doi.org/10.1021/jp4067444.

[22] Y. Wang, X. Ma, L. Lu, Y. He, X. Qi, Y. Deng, Carbon supported MnO_x–Co_3O_4 as cathode catalyst for oxygen reduction reaction in alkaline media, Int. J. Hydrogen Energy 38 (2013) 13611–13616, http://dx.doi.org/10.1016/j.ijhydene.2013.08.048.

[23] J. Xu, P. Gao, T.S. Zhao, Non-precious Co_3O_4 nano-rod electrocatalyst for oxygen reduction reaction in anion-exchange membrane fuel cells, Energy Environ. Sci. 5 (2012) 5333, http://dx.doi.org/10.1039/c1ee01431e.

[24] S. Shan, J. Luo, L. Yang, C.-J. Zhong, Nanoalloy catalysts: structural and catalytic properties, Catal. Sci. Technol. (2014), http://dx.doi.org/10.1039/C4CY00469H.

[25] J.-H. Jang, E. Lee, J. Park, G. Kim, S. Hong, Y.-U. Kwon, Rational syntheses of core–shell Fex@Pt nanoparticles for the study of electrocatalytic oxygen reduction reaction, Sci. Rep. 3 (2872) (2013), http://dx.doi.org/10.1038/srep02872.

[26] F. Godínez-Salomón, M. Hallen-López, O. Solorza-Feria, Enhanced electroactivity for the oxygen reduction on Ni@Pt core–shell nanocatalysts, Int. J. Hydrogen Energy 37 (2012) 14902–14910, http://dx.doi.org/10.1016/j.ijhydene.2012.01.157.

[27] Q.-H. Zhang, W.-H. Yang, H.-H. Wang, M.-Q. Wang, C.-J. Cai, Facile synthesis of platinum alloy nanoparticles with enhanced activity for ethylene glycol electro-oxidation, ECS Electrochem. Lett. 3 (2014) F73–F75, http://dx.doi.org/10.1149/2.0031412eel.

[28] L. Han, P. Cui, H. He, H. Liu, Z. Peng, J. Yang, A seed-mediated approach to the morphology-controlled synthesis of bimetallic copper-platinum alloy nanoparticles with enhanced electrocatalytic performance for the methanol oxidation reaction, J. Power Sources 286 (2015) 488–494, http://dx.doi.org/10.1016/j.jpowsour.2015.04.003.

[29] C. Zhang, S.Y. Hwang, A. Trout, Z. Peng, Solid-state chemistry-enabled scalable production of octahedral Pt–Ni alloy electrocatalyst for oxygen reduction reaction, J. Am. Chem. Soc. 136 (2014) 7805–7808, http://dx.doi.org/10.1021/ja501293x.

[30] X. Zhao, S. Chen, Z. Fang, J. Ding, W. Sang, Y. Wang, et al., Octahedral Pd@Pt 1.8 Ni core–shell nanocrystals with ultrathin PtNi alloy shells as active catalysts for oxygen reduction reaction, J. Am. Chem. Soc. 137 (2015) 2804–2807, http://dx.doi.org/10.1021/ja511596c.

[31] Y.-J. Wang, N. Zhao, B. Fang, H. Li, X.T. Bi, H.g Wang, Carbon-supported Pt-Based alloy electrocatalysts for the oxygen reduction reaction in polymer electrolyte membrane fuel cells: particle size, shape, and composition manipulation and their impact to activity, Chem. Rev. (2015), http://dx.doi.org/10.1021/cr500519c, 150414100746000.

[32] X. Huang, L. Cao, Y. Chen, E. Zhu, Z. Lin, M. Li, et al., High-performance transition metal-doped Pt_3Ni octahedra for oxygen reduction reaction, Science (80) (2014) 4489.

[33] L. Gan, C. Cui, M. Heggen, F. Dionigi, S. Rudi, P. Strasser, Element-specific anisotropic growth of shaped platinum alloy nanocrystals, Science (80) (2014) 346.

[34] T.R. Cook, D.K. Dogutan, S.Y. Reece, Y. Surendranath, T.S. Teets, D.G. Nocera, Solar energy supply and storage for the legacy and nonlegacy worlds, Chem. Rev. 110 (2010) 6474–6502, http://dx.doi.org/10.1021/cr100246c.

[35] M. Higashi, K. Domen, R. Abe, Fabrication of an efficient BaTaO2N photoanode harvesting a wide range of visible light for water splitting, J. Am. Chem. Soc. 135 (2013) 10238–10241, http://dx.doi.org/10.1021/ja404030x.

[36] T. Ohno, L. Bai, T. Hisatomi, K. Maeda, K. Domen, Photocatalytic water splitting using modified GaN:ZnO solid solution under visible light: long-time operation and regeneration of activity, J. Am. Chem. Soc. (2012), http://dx.doi.org/10.1021/ja302479f.

[37] J. Su, L. Guo, N. Bao, C.A. Grimes, Nanostructured WO_3/$BiVO_4$ heterojunction films for efficient photoelectrochemical water splitting, Nano Lett. 11 (2011) 1928–1933, http://dx.doi.org/10.1021/nl2000743.

[38] A. Grimaud, K.J. May, C.E. Carlton, Y.-L. Lee, M. Risch, W.T. Hong, et al., Double perovskites as a family of highly active catalysts for oxygen evolution in alkaline solution, Nat. Commun. 4 (2013) 2439, http://dx.doi.org/10.1038/ncomms3439.

[39] J. Suntivich, K.J. May, H.A. Gasteiger, J.B. Goodenough, Y. Shao-Horn, A Perovskite Oxide Optimized for Oxygen Evolution Catalysis from Molecular Orbital Principles, Science 334 (80) (2011) 1383–1385, http://dx.doi.org/10.1126/science.1212858.

[40] Y. Zhu, W. Zhou, Z.-G. Chen, Y. Chen, C. Su, M.O. Tadé, et al., SrNb 0.1Co 0.7 Fe 0.2 O 3-δ Perovskite as a Next-Generation Electrocatalyst for Oxygen Evolut, Angew. Chemie Int. Ed. (2015), http://dx.doi.org/10.1002/anie.201408998, n/a–n/a.

[41] Y. Zhu, W. Zhou, Y. Chen, J. Yu, X. Xu, C. Su, et al., Boosting oxygen reduction reaction activity of palladium by stabilizing its unusual oxidation states in perovskite, Chem. Mater. 27 (2015) 3048–3054, http://dx.doi.org/10.1021/acs.chemmater.5b00450.

[42] J.M. Jaksic, D. Labou, G.D. Papakonstantinou, A. Siokou, M.M. Jaksic, Novel spillover interrelating reversible electrocatalysts for oxygen and hydrogen electrode reactions, J. Phys. Chem. C 114 (2010) 18298–18312, http://dx.doi.org/10.1021/jp105491k.

[43] V.T.T. Ho, C.J. Pan, J. Rick, W.N. Su, B.J. Hwang, Nanostructured $Ti_{0.7}Mo_{0.3}O_2$ support enhances electron transfer to Pt: high-performance catalyst for oxygen reduction reaction, J. Am. Chem. Soc. 133 (2011) 11716–11724, http://dx.doi.org/10.1021/ja2039562.

[44] Y. Zhu, C. Su, X. Xu, W. Zhou, R. Ran, Z. Shao, A universal and facile way for the development of superior bifunctional electrocatalysts for oxygen reduction and evolution reactions utilizing the synergistic effect, Chem. – A Eur. J. 20 (2014) 15533–15542, http://dx.doi.org/10.1002/chem.201403192.

[45] Y. Huang, J. Zhang, A. Kongkanand, F.T. Wagner, J.C.M. Li, J. Jorne, Transient platinum oxide formation and oxygen reduction on carbon-supported platinum and platinum–cobalt alloy electrocatalysts, J. Electrochem. Soc. 161 (2013) F10–F15, http://dx.doi.org/10.1149/2.018401jes.

[46] S. Shan, J. Luo, J. Wu, N. Kang, W. Zhao, H. Cronk, et al., Nanoalloy catalysts for electrochemical energy conversion and storage reactions, RSC Adv. 4 (2014) 42654–42669, http://dx.doi.org/10.1039/c4ra05943c.

[47] J.D. Blakemore, H.B. Gray, J.R. Winkler, A.M. Müller, Co_3O_4 nanoparticles made by pulsed-laser ablation in liquids as high activity catalysts for water oxidation, ACS Catal. 3 (2013) 2497–2500.

[48] G. Ledoux, D. Amans, C. Dujardin, K. Masenelli-Varlot, Facile and rapid synthesis of highly luminescent nanoparticles via pulsed laser ablation in liquid, Nanotechnology 20 (2009) 445605, http://dx.doi.org/10.1088/0957-4484/20/44/445605.

[49] L. Liao, Q. Zhang, Z. Su, Z. Zhao, Y. Wang, Y. Li, et al., Efficient solar water-splitting using a nanocrystalline CoO photocatalyst, Nat. Nanotechnol. 9 (2014) 69–73, http://dx.doi.org/10.1038/nnano.2013.272.

[50] V. Amendola, M. Meneghetti, Laser ablation synthesis in solution and size manipulation of noble metal nanoparticles, Phys. Chem. Chem. Phys. 11 (2009) 3805–3821, http://dx.doi.org/10.1039/b900654k.

[51] G. Cristoforetti, E. Pitzalis, R. Spiniello, R. Ishak, M. Muniz-Miranda, Production of palladium nanoparticles by pulsed laser ablation in water and their characterization, J. Phys. Chem. C 115 (2011) 5073–5083, http://dx.doi.org/10.1021/jp109281q.

[52] V. Amendola, P. Riello, M. Meneghetti, Magnetic nanoparticles of iron carbide, iron oxide, iron@iron oxide, and metal iron synthesized by laser ablation in organic solvents, J. Phys. Chem. C 115 (2011) 5140–5146, http://dx.doi.org/10.1021/jp109371m.

[53] K. Hagedorn, B. Liu, A. Marcinkevicius, Intermetallic PtPb nanoparticles prepared by pulsed laser ablation in liquid, J. Electrochem. Soc. 160 (2013) F106.

[54] T.B. Hur, T.X. Phuoc, M.K. Chyu, Synthesis of Mg–Al and Zn–Al-layered double hydroxide nanocrystals using laser ablation in water, Opt. Lasers Eng. 47 (2009) 695–700, http://dx.doi.org/10.1016/j.optlaseng.2008.11.006.

[55] E. Jiménez, K. Abderrafi, R. Abargues, J.L. Valdés, J.P. Martínez-Pastor, Laser-ablation-induced synthesis of SiO_2-capped noble metal nanoparticles in a single step, Langmuir 26 (2010) 7458–7463, http://dx.doi.org/10.1021/la904179x.

[56] H. Zeng, W. Cai, J. Hu, G. Duan, P. Liu, Y. Liu, Violet photoluminescence from shell layer of Zn/ZnO core–shell nanoparticles induced by laser ablation, Appl. Phys. Lett. 88 (2006) 171910, http://dx.doi.org/10.1063/1.2196051.

[57] K.Y. Niu, J. Yang, S.A. Kulinich, J. Sun, X.W. Du, Hollow nanoparticles of metal oxides and sulfides: fast preparation via laser ablation in liquid, Langmuir 26 (2010) 16652–16657, http://dx.doi.org/10.1021/la1033146.

[58] S. Hu, C. Melton, D. Mukherjee, A facile route for the synthesis of nanostructured oxides and hydroxides of cobalt using laser ablation synthesis in solution (LASIS), Phys. Chem. Chem. Phys. 16 (2014) 24034–24044, http://dx.doi.org/10.1039/c4cp03018d.

[59] A. Miotello, R. Kelly, Laser-induced phase explosion: new physical problems when a condensed phase approaches the thermodynamic critical temperature, Appl. Phys. A Mater. Sci. Process. 69 (1999) 67–73, http://dx.doi.org/10.1007/s003399900296.

[60] V. Amendola, M. Meneghetti, What controls the composition and the structure of nanomaterials generated by laser ablation in liquid solution? Phys. Chem. Chem. Phys. 15 (2012) 3027–3046, http://dx.doi.org/10.1039/c2cp42895d.

[61] P. Wagener, S. Ibrahimkutty, A. Menzel, A. Plech, S. Barcikowski, Dynamics of silver nanoparticle formation and agglomeration inside the cavitation bubble after pulsed laser ablation in liquid, Phys. Chem. Chem. Phys. 15 (2013) 3068–3074, http://dx.doi.org/10.1039/c2cp42592k.

[62] Y. Sun, Y. Xia, Mechanistic study on the replacement reaction between silver nanostructures and chloroauric acid in aqueous medium mechanistic study on the replacement reaction between silver nanostructures and chloroauric acid in aqueous, J. Am. Chem. Soc. (2004) 3892–3901, http://dx.doi.org/10.1021/ja039734c.